

Contents lists available at ScienceDirect

International Journal of Applied Earth Observation and Geoinformation

journal homepage: www.elsevier.com/locate/jag





Exploring the potential of multi-source satellite remote sensing in monitoring crop nutrient status: A multi-year case study of cranberries in Wisconsin, USA

Yurong Huang ^a, Nanfeng Liu ^{a,*}, Erin Wagner Hokanson ^b, Nicole Hansen ^c, Philip A. Townsend ^d

- ^a Carbon-Water Research Station in Karst Regions of Northern, Guangdong Provincial Key Laboratory of Urbanization and Geo-simulation, School of Geography and Planning, Sun Yat-sen University, Guangzhou, 510275, China
- ^b Space Science and Engineering Center, University of Wisconsin-Madison, Madison, WI 53715, USA
- Cranberry Creek Cranberries, Inc., Necedah, WI 54646, USA
- ^d Department of Forest and Wildlife Ecology, University of Wisconsin-Madison, Madison, WI 53705, USA

ARTICLE INFO

Keywords: Crop foliar nutrients Multi-source satellite remote sensing Machine learning Precision nutrient management

ABSTRACT

A timing and precise diagnosis of crop nutrient status is essential for optimizing management practices that promote environmentally friendly and enhanced crop yields. Although plant tissue analysis has conventionally been employed to evaluate the nutritional status of crops, this method cannot capture the spatial variability of crop nutrients. In contrast, satellite-based remote sensing can monitor the nutrient status of crops across expansive areas. This study explored the capability of multi-source satellite images (PlanetScope-4: 3 m, 4 bands; PlanetScope-8: 3 m, 8 bands; Sentinel-2: 10-60 m, 13 bands; PRISMA: 30 m, 239 bands) in mapping 12 foliar nutrients in cranberries. Three machine learning approaches, including partial least squared regression (PLSR), support vector regression (SVR), random forest regression (RFR), were used to relate foliar nutrients to different types of satellite-derived features (SR: surface reflectance; VI: vegetation indices; TF: texture features) or their combinations (SR+VI, VI+TF and SR+VI+TF). Model performance was compared across different foliar nutrients, modelling approaches and combinations of model input features using R^2 (the coefficient of determination) and RRMSE (relative root mean square error, = root mean square error/nutrient range × 100 %). Input features that were important to foliar nutrient modelling were identified. The model performance difference among nutrients was consistent between Planet-4 and Sentinel-2, as well as between Planet-8 and PRISMA. In the Planet-4 and Sentinel-2 derived models, N was best predicted (average R² = 0.77, average RRMSE=15 %), followed by macronutrients S (0.60-0.63, 11 %), Mg (0.58-0.65, 10-11 %), Ca (0.49-0.51, 9 %), Na (0.69, 22 %), P (0.49, 9 %) and K (0.20, 8 %), and then by all micronutrients (i.e., Fe, Mn, B, Cu and Zn: $R^2 = 0.04-0.61$; RRMSE=16-28 %). In the Planet-8 and PRISMA derived models, macronutrients (i.e., N, P, K, Mg, Ca, S and Na) had lower R^2 and RRMSE ($R^2 = 0.06-0.59$; RRMSE=7-57 %) than micronutrients (i.e., Fe, Mn, B, Cu and Zn: $R^2 = 0.18-0.60$; RRMSE=19-66 %). The successful retrieval of foliar nutrients from satellite imagery was influenced by many factors, including the intercorrelation between nutrients and model input features, the data availability at critical growth stages, and satellite images characteristics (e.g., spatial and spectral resolutions). Except for foliar nitrogen, foliar nutrients typically do not exhibit distinct absorption features associated with C, H, N, or O molecular bonds in the 400-2500 nm range. Our results indicate that their successful retrieval can be primarily attributed to the association between foliar nutrients and other leaf components (e.g., pigments, water, and dry matter) that do display spectral features within this range. Our study demonstrated the potential of integrating multi-source satellite data for precise nutrient monitoring over large scales.

E-mail address: liunf3@mail.sysu.edu.cn (N. Liu).

 $^{^{\}star}$ Corresponding author.

1. Introduction

Depending on the relative quantities in crops, mineral nutrients are generally grouped into macro- and micro-nutrients (Kirkby, 2023). Take the cranberry crop investigated in our study as an example. The macronutrients include nitrogen (N), phosphorus (P), potassium (K), magnesium (Mg), calcium (Ca) and sulfur (S), while the micro-nutrients include iron (Fe), manganese (Mn), boron (B), copper (Cu), zinc (Zn). These nutrients are essential to crop growth, production and quality (Brown et al., 2022; Connor et al., 2011; de Bang et al., 2021; Taiz and Zeiger, 2010; Thapa et al., 2021). Primary macronutrients N, P and K play a fundamental role in crop development such as energy metabolism/storing, protein/fat/glucose synthesis, root growth and water intake. Secondary macronutrients Mg, Ca, S regulate several critical processes such as the formation of chlorophyll, the absorption/transportation of phosphorus and the activating of enzymes. Although being needed in relatively small quantities by crops, micronutrients are responsible for several essential functions such as sugar shipment, flowering, fruiting, enzyme composition and chloroplast production. Any deficiency or excess of mineral nutrients in crops may result in symptoms of chlorosis and necrosis (de Bang et al., 2021; Francis et al., 2023), vield reduction (Amanullah, 2020; Li et al., 2019) and even environmental pollution (Barker and Pilbeam, 2015; Campos-Soriano et al. (2020); Van Maarschalkerweerd and Husted, 2015). Therefore, an accurate diagnosis of crop nutrient status is needed to optimize management practices for environmental-friendly crop yields.

Plant tissue analysis helps determine the nutritional status of plants and diagnose any deficiencies or excesses of essential elements necessary for their growth and development (Jones and Case, 1990; Marschner, 1995; Mortvedt, 1991; Muñoz-Huerta et al., 2013). This technique requires an in-field destructive collection and a laboratory chemical examination of plant tissues (e.g., foliage, petioles and stems), and therefore is time-consuming and laborious (Adhikari et al., 2020). Furthermore, since plant tissues are collected at spatially limited and separated sites, this method cannot represent the spatial variation in crop nutrients (Berger et al., 2020). Thus, plant tissue analysis is inappropriate to guide management practices for those unsampled areas.

Satellite remote sensing enables the monitoring of the entire nutritional life cycle of crops across expansive regions, due to its high flight altitude and long flight endurance (Berger et al., 2020; Weiss et al., 2020). Ideally, satellite images with high spatial, temporal and spectral resolutions are preferred for monitoring the nutrient status of crops. However, achieving such high resolutions in all three domains simultaneously poses significant technical and practical challenges, often necessitating trade-offs among these parameters. Take the satellite imagery used our study as an example. PlanetScope imagery offers a high spatial resolution of ~ 4 m and a remarkable temporal resolution of one day. However, it is limited to $4 \sim 8$ spectral bands within the 400-1000nm wavelength range. In contrast, Sentinel-2 imagery features a moderate spatial resolution ranging from 10 to 60 m and a temporal resolution of 5 days, yet it encompasses 13 spectral bands spanning the 400-2500 nm wavelength range. The hyperspectral PRISMA imagery has the highest spectral resolution (240 bands, ~10 nm bandwidth) within 400–2500 nm, while its spatial resolution (\sim 30 m) and revisiting period (~29 days) are relatively poor. Each satellite imagery platform offers distinct advantages and limitations for agricultural monitoring applications, particularly in retrieving crop nutrient information. However, a comprehensive comparison of their capabilities in this regard remains under-investigated.

Various data-driven models have been used to quantitatively relate crop nutrient concentrations to satellite-observed spectral signals, including Partial Least Squared Regression (PLSR) (Belgiu et al., 2023; Inoue et al., 2012; Liu et al., 2021), Support Vector Regression (SVR) (Cao et al., 2022; Sarkar et al., 2023), and Random Forest Regression (RFR) (Osco et al., 2020; Pereira (2022)). PLSR projects input features into a new orthogonal space (also called latent factors), and then

regresses these latent factors against crop nutrients. SVR maps input features into a high-dimensional feature space, where the optimal hyperplane is found to fit the data within a specified margin of error, minimizing the overall prediction error while maintaining computational efficiency. RFR is a machine learning algorithm that uses an ensemble of decision trees to predict continuous outcomes. By averaging the predictions of multiple trees. RFR improves accuracy and reduces overfitting, making it robust against noise in the data.

Various types of features have been used by statistical models to predict crop nutrients, including: 1) Spectral Reflectance (SR); 2) Vegetation Indices (VI); 3) Texture Features (TF). Some studies have found that incorporating more spectral bands into model inputs could improve prediction accuracy (Cao et al., 2022; Darvishzadeh et al., 2019; Delloye et al., 2018; Liu et al., 2021). For example, Delloye et al. (2018) demonstrated a substantial improvement in model accuracy by incorporating the four Sentinel-2 red-edge spectral bands into models, surpassing the performance of models that only used the four 10 m spectral bands as inputs. Belgiu et al. (2023) demonstrated that hyperspectral PRISMA satellite (239 bands in 400–2500 nm) was generally better than multispectral Sentinel-2 satellites (13 bands in 400–2500 nm) in predicting the grain nutrient composition of staple crops. This is mainly because hyperspectral satellites can detect the finer spectral features related to crop nutrient changes.

Vegetation indices, a mathematical combination of few spectral bands, have been widely used for modelling crop foliar nutrients due to its simplicity and effectiveness (Zeng et al., 2022). Sharifi (2020) evaluated the performance of ten commonly used VIs derived from Sentinel-2 images in predicting maize nitrogen uptake, and found that VIs utilizing near-infrared and red-edge spectral bands had a better prediction accuracy than other VIs. Belgiu et al. (2023) tested all possible Sentinel-2 band combinations on the normalized difference spectral index (NDSI). They found that the optimal band combination for estimating nutrients in staple crop grains varied from conditions such as crop types, growth stages and grain nutrients. Liu et al. (2021) grouped 24 commonly used hyperspectral VIs into three classes according to their responsiveness to leaf biochemistries (i.e., leaf pigments, water and dry matter), and found that no group of vegetation indices outperformed others in predicting potato leaf nitrogen. All these findings confirmed that the fact that there was no optimal VI for modelling crop nutrients.

Texture features have proven to be valuable attributes for capturing the spatial variations in crop nutrient concentrations, especially when working with high-resolution images (Fan et al., 2023; Liu et al., 2018; Zheng et al., 2020). Gray-level co-occurrence matrix (GLCM) texture features are typically used to quantify the texture of an image by examining the spatial relationships between pixel intensities. These features provide information about the texture's patterns, contrast, homogeneity, and other characteristics, which cannot be captured by simply analyzing individual pixels. For example, Zheng et al. (2020) calculated all possible normalized difference texture indices (NDTI) based on UAV multispectral images. They found that NDTI had comparable performance with traditional VIs in predicting rice nitrogen nutrient. Currently, most research is focused on extracting texture features from UAV images, while relatively few studies employed satellite images of high spatial resolutions such as PlanetScope, WorldView and QuickBird (Sarkar et al., 2023). The capability of high-resolution satellite images to characterize the spatial variations in crop nutrient concentrations remains under-investigated.

Previous studies have shown that a combination of various features can improve model performance (Fan et al., 2022; Fu et al., 2020; Pereira (2022); Zheng et al., 2020). For example, Fan et al. (2023) extracted eight gray-level co-occurrence matrix (GLCM) texture features from unmanned aerial vehicle images with a spatial resolution of 1.3 cm. They found an improvement in the prediction accuracy of potato leaf nitrogen models by integrating these texture features alongside spectral features. Similar findings were also reported by Zheng et al. (2020) and Pereira (2022), emphasizing the significance of integrating spatial and

spectral information to enhance the prediction of foliar nutrients.

In this study, we aim to examine the capability of multi-source satellite images with various spatial and spectral resolutions to monitor the foliar nutrient status in cranberries. More specifically, we: 1) investigate the capability of PlanetScope, Sentinel-2 and PRISMA images to quantify 12 nutrients in cranberry leaves; 2) identify the optimal features for predicting nutrients; 3) evaluate the performance of different modelling approaches in predicting foliar nutrients.

2. Study site and data collection

2.1. Study site

As the top cranberry growing state in the US, Wisconsin harvested half of the nation's cranberry supply (USDA, 2022). Our field sampling was conducted at a cranberry farm in Wisconsin, USA (Fig. 1). It has 210 commercial cranberry beds (size: 50×300 m), and maintains 12 cranberry cultivars. In Wisconsin, mid-May to early September is the cranberry growing season: Buds begin to form from mid to late May, coupled with some elongation of stalks and leaves; Flowers emerge in late June, lasting for a month into July; Fruits undergo maturation for 2–3 months, varying based on cultivars and weather conditions; Harvesting commences in late September and extends into October.

2.2. Foliar nutrients

Foliar samples were collected from 278 cranberry beds during the growing seasons of 2018–2021 ("Foliar nutrients" in Table 1). Within each cranberry bed, 20 cranberry uprights were randomly collected. These samples underwent drying at 65 °C for at least three days, followed by grinding to ensure passage through a 20-mesh sleeve (0.25 mm). Twelve nutrients were chemically analyzed, including seven foliar macronutrients (i.e., N, P, K, Mg, Ca, S and Na) and five foliar micronutrients (i.e., Fe, Mn, B, Cu and Zn) (Liu et al. 2023). Nitrogen was determined using the Dumas combustion method. For others, the powders underwent digestion with nitric acid and hydrogen peroxide, followed by a chemical analysis on an inductively coupled plasma-optical emission spectrometer.

2.3. Multi-source satellite imagery

The capability of four types of satellite images to monitor 12 cranberry foliar nutrients was investigated, including PlanetScope-4, PlanetScope-8, Sentinel-2 and PRISMA (Table 1). The PlanetScope constellation consists of ~ 130 Dove cube-satellites, and has the capacity to image the global land surface every day (Roy et al., 2021) ("Planet-Scope-4 and -8" in Table 1). Three generations of satellites have been launched during the PlanetScope mission. The first two generations, Dove-C and -R, provide four spectral bands within 400–900 nm

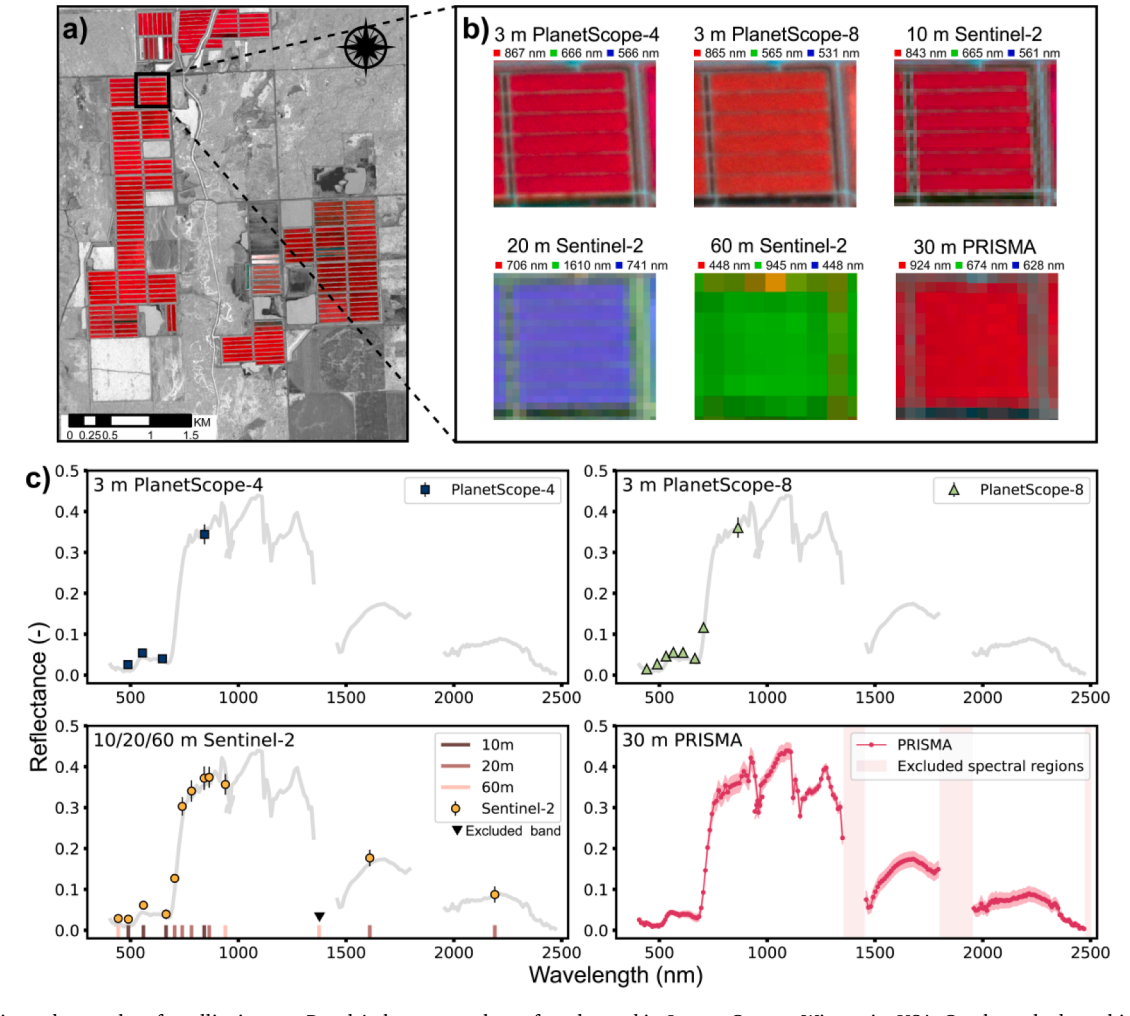


Fig. 1. Study site and examples of satellite images. Panel A shows a cranberry farm located in Juneau County, Wisconsin, USA. Cranberry beds are highlighted by the false color composite of a PlanetScope-4 image. Panel B shows the close-up views of six cranberry beds (i.e., the black box in panel A with different color composites from Sentinel-2, PlanetScope-4, PlanetScope-8 and PRISMA images. Panel C shows the average spectra (±one standard derivation) of all cranberry beds extracted from these satellite images.

Table 1Data used in the project.

| A)Foliar nutrients | s | | | | |
|---------------------------|------------------------------------|-----------------|--------------------------------------|---------------------------|--|
| Sampling date | Sample si | ze | Foliar nutrients | | |
| 2018-07-03 | 79 | | Macro-nutrients: N, P, K, Mg, Ca, S, | | |
| 2019–06-26 | 75 | | Na; | | |
| 2019–09-04 | 31 | | | e, Mn, B, Cu, and Zn; | |
| 2020–08-15 | 41 | | Unit: mg•g-1 | | |
| 2021–06-22 | 11 | | | | |
| 2021–08-15 | 41 | | | | |
| B) PlanetScope-4 | | | 0 . 1 | 01 | |
| Acquisition date | Band ID | Band name | Spectral range (nm) | Spatial resolution (m) | |
| 2018-07-02 | 1 | Blue | 455-515/ | 3.0-4.1 | |
| 2019-06-22 | | | 464-517 | | |
| 2019-08-30 | 2 | Green | 500-590/ | | |
| 2020-08-12 | | | 547–585 | | |
| 2021-06-18 | 3 | Red | 590-670/ | | |
| | | | 650-682 | | |
| | 4 | Near | 780–860/ | | |
| | | infrared | 846–888 | | |
| C) Sentinel-2 A/B | | n 1 | 0 | 0 | |
| Acquisition | Band ID | Band | Spectral range | Spatial | |
| date 2021–06-18 | 1D 1 | name Coastal | (nm) 431–452 | resolution (m) 3.7–4.2 | |
| 2021-06-18 | 1 | blue | 431–432 | 3.7-4.2 | |
| 2021-00-13 | 2 | Blue | 465–515 | | |
| | 3 | Green | 513–549 | | |
| | 4 | Green | 547–583 | | |
| | 5 | Yellow | 600–620 | | |
| | 6 | Red | 650-680 | | |
| | 7 | Red edge | 697-713 | | |
| | 8 | Near | 845–885 | | |
| | | infrared | | | |
| D) PlanetScope-8 | | | | | |
| Acquisition | Band | Band | Spectral range | Spatial | |
| date | ID | name | (nm) | resolution (m) | |
| 2018–07-08 2019–06-18 | 2 | Blue Green | 458–523 543–578 | 10 | |
| 2019-00-16 | 4 | Red | 650–680 | | |
| 2020–08-11 | 8 | Near | 785–900 | | |
| 2021-06-12 | Ü | infrared | 700 300 | | |
| | 5 | Red edge | 698-713 | 20 | |
| | 6 | Red edge | 733-748 | | |
| | 7 | Red edge | 773-793 | | |
| | 8A | Red edge | 848-880 | | |
| | 11 | SWIR | 1565–1655 | | |
| | 12 | SWIR | 2100-2280 | | |
| | 1 | Coastal blue | 443–453 | 60 | |
| | 9 | Water vapor | 935–955 | | |
| | 10 | SWIR- | 1360–1390 | | |
| E) PRISMA | | Cirrus | | | |
| Acquisition date | Specifications | | VNIR sensor | SWIR sensor | |
| 2021–06-17 | Spectral range (nm) | | 400–1010 | 920-2500 | |
| 2021-08-13 | Number of bands Full width at half | | 66 | 174 | |
| | | | 13 | 13 | |
| | maximum (nm) | | | | |
| | Spatial res | solution (m) | 37.11 | 38.38 | |

("PlanetScope-4" in Table 1), and have a ground sample distance of 3.0–4.1 m. The third generation, SuperDove, provides eight bands within 400–900 nm and has a ground sample distance of 3.7–4.2 m ("PlanetScope-8" in Table 1). In the following sections, PlanetScope images from the first two generations were referred to as PlanetScope-4, while the third generation as PlanetScope-8. In this study, five cloud-free PlanetScope images were found for PlanetScope-4 and two cloud-free images were found for PlanetScope-8 (WWW: https://www.planet.com/explorer/). PlanetScope images had been geometrically orthorectified, atmospherically corrected and spectrally harmonized to the corresponding Sentinel-2 spectral bands (Planet Labs, 2022).

The Sentinel-2 constellation has two satellites Sentinel-2A and -B,

providing a revisit interval of 5 days. Both satellites have thirteen spectral bands within 400–2500 nm and a ground sample distance from 10 to 60 m ("Sentinel-2" in Table 1). Five Sentinel-2 top-of-atmosphere (TOA) images were downloaded (WWW: https://earthexplorer.usgs. gov/). The Sen2Cor package (WWW: https://step.esa.int/main/snap-supported-plugins/sen2cor/, version =2.5) was implemented to correct the atmospheric, topographic, and cirrus effects on TOA images to produce bottom-of-atmosphere (BOA) reflectance images. The BOA images at 20 and 60 m resolutions were spatially resampled to 10 m with the nearest sampling method. The SWIR-Cirrus spectral band (wavelength range: 1360–1390 nm) was excluded because of the absorption by atmospheric water vapor (see the "excluded band" in Fig. 1C).

PRISMA is an Italian Space Agency mission which aims to demonstrate the development and delivery of hyperspectral imagery products (Cogliati et al., 2021). PRISMA consists of two imaging spectrometers: visible-to-near infrared (VNIR) and shortwave infrared (SWIR). The VNIR spectrometer provides 66 narrow bands within 400–1010 nm. The SWIR spectrometer has 174 narrow bands within 920–2505 nm ("PRISMA" in Table 1). Both spectrometers have a bandwidth of ~ 13 nm and a ground sample distance of ~ 37 m. In this study, only two cloud-free PRISMA images were available due to the long satellite revisit cycle ($\sim\!29$ days). The downloaded PRISMA Level-2D images (WWW: http://prisma.asi.it/) had been geometrically orthorectified and atmospherically corrected. Spectral bands within 1361–1450 nm, 1803-1949 nm and 2477-2500 nm were excluded because of the strong atmospheric water absorptions.

3. Methods

3.1. Statistical approaches for modelling foliar nutrients

The performance of three commonly used data-driven approaches in modeling foliar nutrients was evaluated, including PLSR, SVR, and RFR. We randomly divided the raw dataset into calibration and validation datasets with a ratio of 3:1. The calibration dataset was used to optimize model parameters, while the validation dataset was to evaluate the performance of prediction models.

Grid search was conducted to determine the optimal parameters for each modeling approach. This method involves testing every possible combination of model parameters on the calibration dataset within the specified parameter ranges, and then selecting the configuration that yields the best performance. The parameters to be optimized for each modeling approach were outlined in Table 2. For PLSR, the number of latent factors was optimized by minimizing the predicted residual sum of squares (PRESS) (Liu et al., 2021). For SVR, the optimal model parameters were determined using the grid search method. The radial basis function (RBF) was used as the SVR kernel function; The penalty coefficient C, kernel coefficient C and margin of tolerance C were exponentially optimized from C to C and C are C and C and

Table 2 The parameter optimization of each modelling approaches. p is the number of the model inputs.

| Models | Parameters | Grid search range |
|--|---|---|
| Partial least square regression (PLSR) | Number of latent factors | 1, 2,30 |
| Support vector regression (SVR) | Kernel function | Radial basis function (RBF) |
| | Penalty coefficient Kernel coefficient | $2^{-15}, 2^{-14},, 2^{16}$ $2^{-5}, 2^{-4},, 2^{6}$ |
| | Margin of tolerance | 10^{-5} , 10^{-4} ,, 10^{4} |
| Random forest regression | Number of trees | 100 |
| (RFR) | Number of regression features | 1, 2,, <i>p</i> /3 |
| | Maximum tree depth | 3, 4,,15 |
| | Minimum number of samples | 5, 10 |

respectively. For RFR, The number of trees was set to 100 as suggested by Belgiu, (2016); The number of regression features was optimized from 1 to one third of the number of model inputs; The maximum tree depth was optimized from 3 to 15; The minimum number of samples was optimized from 5 or 10.

3.2. Input features of foliar nutrient models

In this study, three types of features were used as the inputs of foliar nutrient models: spectral reflectance (SR), vegetation indices (VI) and texture features (TF). The average surface reflectance at each spectral band was extracted for each cranberry bed. Spectral bands strongly influenced by water vapor absorptions were removed. They were band 10 for Sentinel-2 and spectral bands within 1361–1450 nm, 1803–1949 nm and 2477–2500 nm for PRISMA (Table 1). The Sentinel-2 Coastal blue band was also excluded due to its coarse spatial resolution (i.e., 60 m). Finally, spectral reflectance was vector-normalized to reduce the influence of illumination conditions on reflectance (Wang et al., 2020). A set of vegetation indices (VIs) were calculated for Sentinel-2, Planet-Scope-4 and –8 (Table 3). These VIs were previously utilized to estimate different foliar biochemistries (Pereira (2022)).

Gray-level co-occurrence matrix (GLCM) texture features were calculated for PlanetScope-4, PlanetScope-8 and Sentinel-2 images (Table 4). Here, we calculated texture features for all the bands of PlanetScope-4 and PlanetScope-8, but only for the bands 2, 3, 4 and 8 of Sentiniel-2 due to their fine resolution (10 m). First, satellite images within each cranberry bed were linearly rescaled to a grey level of 256. Then, the GLCM-based texture metrices were calculated with the following parameters: pixels offset $p_1=1$; relative orientation $\theta=0^\circ$; window size $p_2=5$ pixels for PlanetScope-4/8 and 3 pixels for Sentinel-2; window moving step $p_3=1$ pixel. Texture metrices included contrast (CON), angular second moment (ASM), correlation (COR), dissimilarity

Table 3 Spectral indices used for predicting foliar nutrients in this study. R_R , R_G , R_B , R_{NIR} indicates the reflectance in the red, green, blue, near-infrared wavelength range respectively. and

| A) Canopy structure sensitive indices | | | | | |
|---------------------------------------|-------------------|---|----------------|--|--|
| Vegetation indices | Abbreviations | Formulas | References | | |
| Normalized | NDVI | $R_{ m NIR}-R_{ m R}$ | (Rouse et al., | | |
| Difference | | $R_{ m NIR} + R_{ m R}$ | 1973) | | |
| Vegetation Index | | | | | |
| Enhanced | EVI | $2.5 \times (R_{\rm NIR} - R_{\rm R})$ | (Huete, | | |
| Vegetation Index | | $R_{\rm NIR} + 6R_{\rm R} - 7.5R_{\rm B} + 1$ | 1997) | | |
| Wide Dynamic | WDRVI | $0.1R_{ m NIR}-R_{ m R}$ | (Gitelson, | | |
| Range Vegetation Index | | $\overline{0.1R_{ m NIR}+R_{ m R}}$ | 2004) | | |
| Ratio Vegetation | RVI | $R_{ m NIR}$ | (Tucker, | | |
| Index | | RR | 1979) | | |
| B) Leaf biochemistry | sensitive indices | -14 | , | | |
| Vegetation indices | Abbreviations | Formulas | References | | |
| Chlorophyll Index | CI_{green} | $R_{ m NIR}$, | (Gitelson | | |
| green | 9 | $\frac{R_{ m NIR}}{R_{ m G}}$ -1 | et al., 2003) | | |
| Chlorophyll | CVI | $R_{\rm NIR}R_{\rm R}$ | (Vincini | | |
| Vegetation Index | | $R_{\rm G}^2$ | et al., 2008) | | |
| Normalized Green | NGRDI | $R_{\rm G}-R_{\rm R}$ | (Tucker, | | |
| Red Difference Index | | $\overline{R_{ m G}+R_{ m R}}$ | 1979) | | |
| Green Leaf Index | GLI | $2R_{\rm G}-R_{\rm R}-R_{\rm B}$ | (Louhaichi | | |
| | | $\frac{2R_{\rm G}+R_{\rm R}+R_{\rm B}}{2R_{\rm G}+R_{\rm R}+R_{\rm B}}$ | et al., 2001) | | |
| Green Normalized | GNDVI | $R_{ m NIR}-R_{ m G}$ | (Huete et al., | | |
| Difference | | $\frac{R_{ m NIR} + R_{ m G}}{R_{ m NIR} + R_{ m G}}$ | 2002) | | |
| Vegetation Index | | | , | | |
| Structure Insensitive | SIPI | $R_{ m NIR}-R_{ m B}$ | (Pen Uelas | | |
| Pigment Index | | $\frac{R_{NIR} + R_{R}}{R_{NIR} + R_{R}}$ | et al., 1995) | | |
| Visible | VARIgreen | $R_{ m G}-R_{ m R}$ | (Gitelson | | |
| Atmospherically | g.cc. | $\frac{R_{\rm G}+R_{\rm R}-R_{\rm B}}{R_{\rm G}+R_{\rm R}-R_{\rm B}}$ | et al., 2002) | | |
| Resistance Index | | | | | |
| green | | | | | |

Adapted from Bhattarai et al. (2023)Zeng et al. (2022).

Table

Texture features used in this study. In these formulas, both i and j indicate the grey levels of pixels; P_{ij} indicates the probability of the grey level values i and j at adjacent pixels; N is the total grey level; μ indicates the mean; σ indicates the standard deviation; ε is a small positive number (=2.2 \times 10⁻¹⁶). For the symmetrical GLCM, $\sigma_i = \sigma_j$ and $\mu_i = \mu_j$.

| Texture features | Abbreviations | Formulas |
|-----------------------|---------------|---|
| Contrast | CON | $\sum_{i,j=0}^{N-1} P_{ij}(i-j)^2$ |
| Correlation | COR | $\sum_{i,j=0}^{N-1} P_{ij} \left[\frac{(i-\mu_i) \left(j-\mu_j\right)}{\sqrt{(\sigma_i^2)(\sigma_j^2)}} \right]$ |
| Dissimilarity | DIS | $\sum_{i,j=0}^{N-1} P_{ij} i-j $ |
| Angular second moment | ASM | $\sum_{i,j=0}^{N-1} P_{ij}^{2}$ |
| Energy | ENE | $\sqrt{\sum_{i,j=0}^{N-1} {P_{ij}}^2}$ |
| Homogeneity | HOM | $\sum_{i,i=0}^{N-1} P_{ij} i-j $ |
| Mean | MEA | $\mu_i = \sum_{i,j=0}^{N-1} P_{ij} i, \mu_j = \sum_{i,j=0}^{N-1} P_{ij} j$ |
| Variance | VAR | ${\sigma_i}^2 = \sum_{i,j=0}^{N-1} \! P_{ij} (i-\mu_i)^2, {\sigma_j}^2 = $ |
| | | $\sum_{i,j=0}^{N-1} P_{ij} \Bigl(i-\mu_j\Bigr)^2$ |
| Standard deviation | SD | $\sigma_i = \sqrt{{\sigma_i}^2}, \sigma_j = \sqrt{{\sigma_j}^2}$ |
| Sum average | SA | $\sum_{i,j=0}^{N-1} P_{ij}(i+j)$ |
| Entropy | ENT | $\sum_{i,j=0}^{N-1} P_{ij} log_2 \left(P_{ij} + \varepsilon \right)$ |

(DIS), energy (ENE), homogeneity (HOM), mean (MEA), standard deviation (SD), variance (VAR), sum average (SA) and entropy (ENT) (Table 4).

We tested various combinations of the above-mentioned three types of input features (Table 5). For Sentinel-2, PlanetScope-4 and PlanetScope-8, the performance of seven combinations of input features in predicting foliar nutrients was examined, including spectral reflectance (SR), vegetation indices (VI), texture features (TF), SR+VI, SR+TF, VI+TF, and SR+VI+TF; For PRISMA, only spectral reflectance was investigated because of the coarse resolution.

3.3. Model evaluation

The statistical models calibrated in Section 3.1 were applied to the validation datasets. Two indicators were used to evaluate model performance: the coefficient of determination (R^2) and the relative root mean square errors (*RRMSE*):

$$R^{2} = 1 - \frac{\sum_{i=1}^{n} (y_{i} - \widehat{y}_{i})^{2}}{\sum_{i=1}^{n} (y_{i} - \overline{y})^{2}}$$
(1)

$$RRMSE = \frac{\sqrt{\frac{1}{n} \sum_{i=1}^{n} (y_i - \widehat{y}_i)^2}}{y_{max} - y_{min}} \times 100\%$$
(2)

Where n is the number of samples; y_i is the foliar nutrient measurement of the i-th sample; \widehat{y}_i is the predicted nutrient of the i-th sample; \overline{y} is the mean of nutrient measurements; y_{max} and y_{min} are the maximum and minimum of nutrient measurements, respectively.

Furthermore, the feature importance scores from PLSR, SVR and RFR models were calculated to identify the features that were important to nutrient prediction. For PLSR, the standardized regression coefficients were utilized as the metrics of feature importance. For SVR, the inner product of spectral reflectance and the $\alpha\text{-vector}$ was used to evaluate feature importance. For RFR model, the Gini importance coefficients were used to measure the importance of input features. For all metrics, the larger the absolute value of the feature important scores, the more important the feature.

Table 5
Number of variables used in each feature combination. SR: spectral reflectance; VI: vegetation indices; TF: texture features.

| Satellite images | Number of variables used in each feature combination | | | | | | |
|------------------|--|----|----|-------|-------|-------|----------|
| | SR | VI | TF | SR+VI | SR+TF | SR+TF | SR+VI+TF |
| PlanetScope-4 | 4 | 11 | 44 | 15 | 48 | 55 | 59 |
| PlanetScope-8 | 8 | 11 | 88 | 19 | 96 | 99 | 107 |
| Sentinel-2 | 12 | 11 | 44 | 23 | 56 | 55 | 67 |
| PRISMA | 204 | _ | _ | _ | - | _ | - |

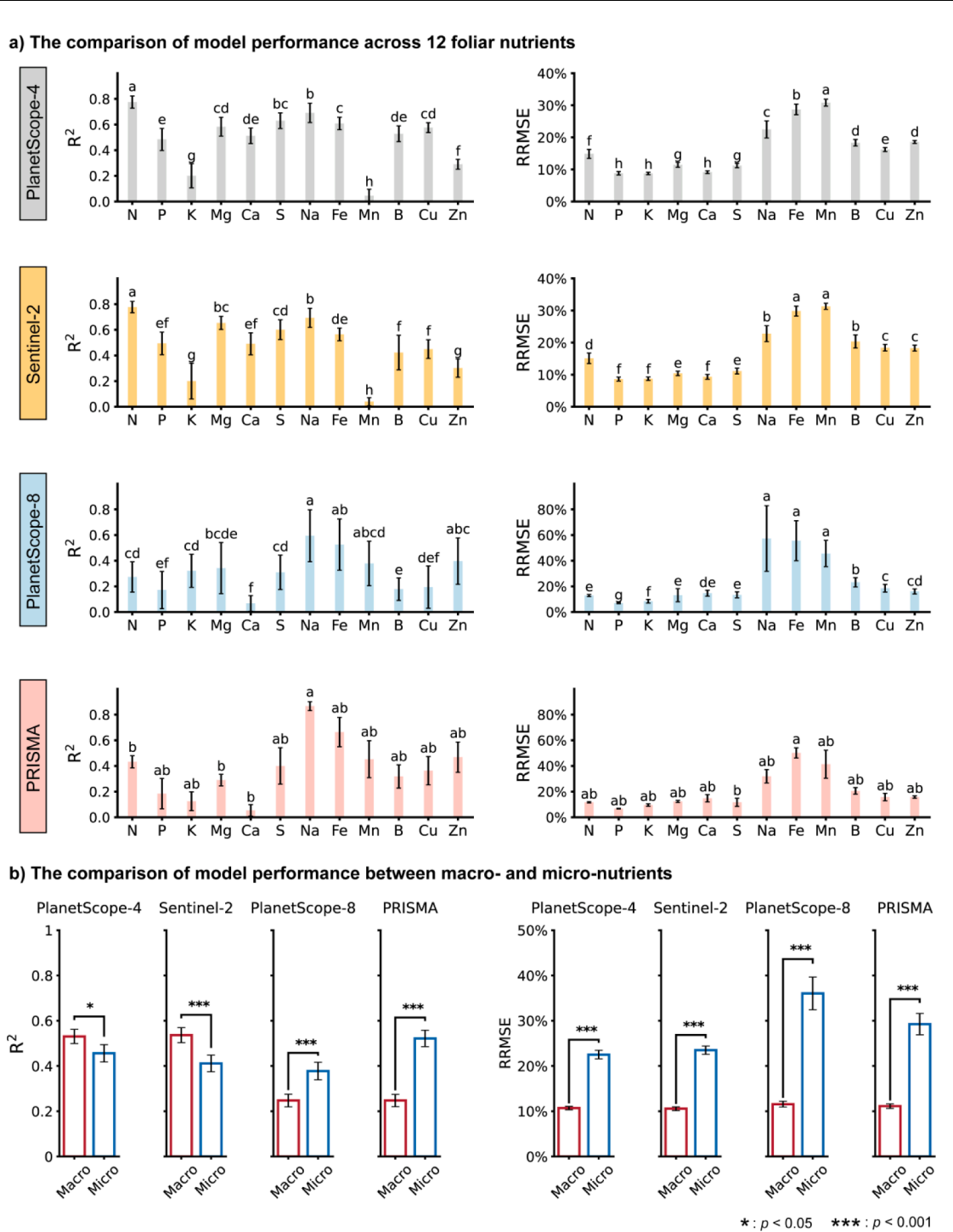


Fig. 2. Comparison of model performance across foliar nutrients. Seven types of input features (Table 5) were fed into each of three modelling approaches (i.e., PLSR, SVR and RFR) for each foliar nutrient. The R^2 and RRMSE values derived from these models were grouped into either 12 foliar nutrients (Panel A) or two nutrient groups (Panel B). Bars indicate the average \pm one standard derivation of R^2 and RRMSE values within each group. Panel A shows the model performance comparison among 12 foliar nutrients. Welch ANOVA indicates that both R^2 and RRMSE are significantly different among 12 foliar nutrients (p < 0.001). The Tamhane p = 0.001 are two used to rank p = 0.001 and RRMSE in descending order (indicated by alphabets a-h). Panel B shows the comparison of model performance between macronutrients (p = 0.001). The Mann-Whitney U test indicates that both model p = 0.001 and RRMSE are significantly different between macronutrients and micronutrients.

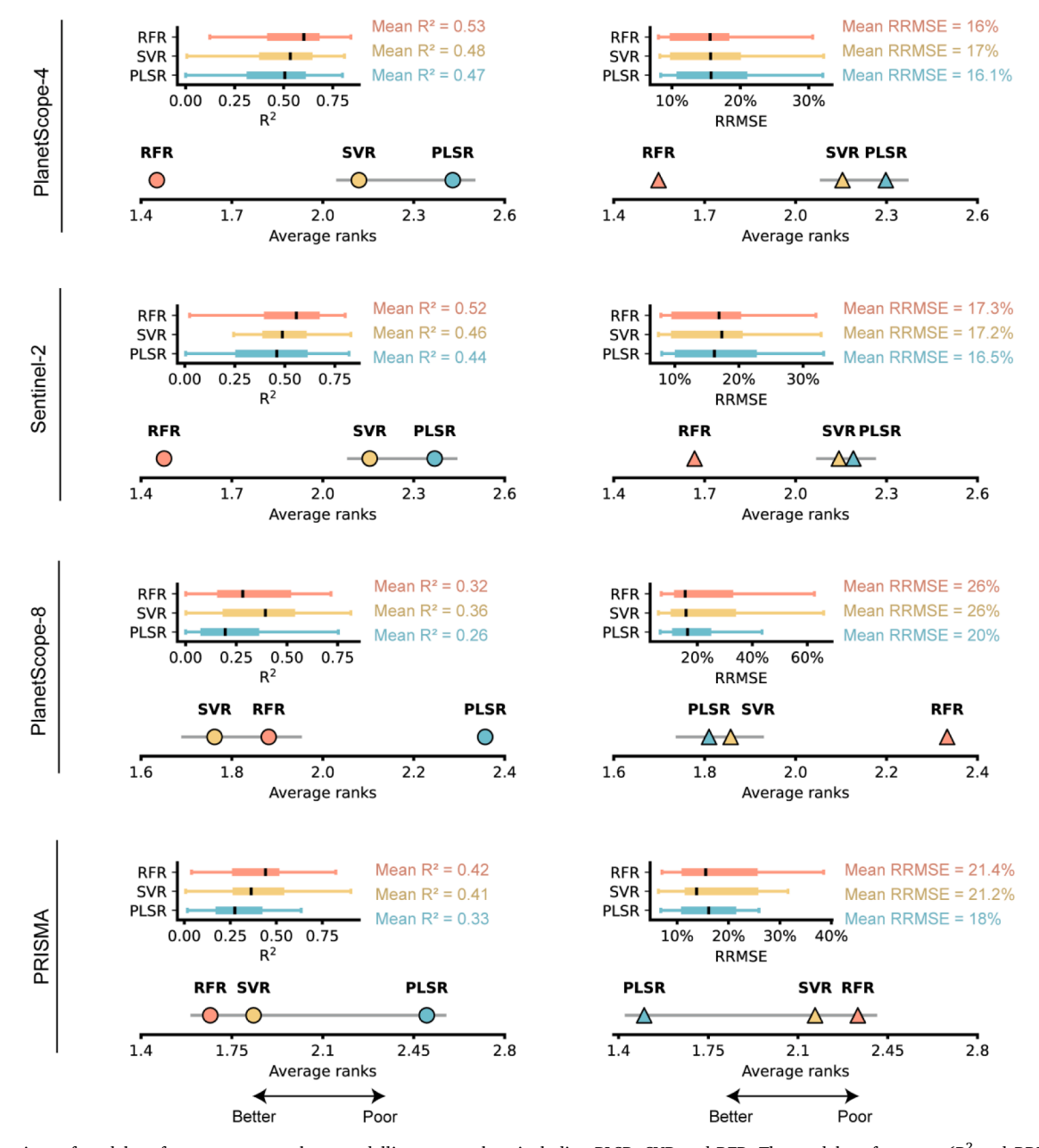


Fig. 3. Comparison of model performance among three modelling approaches, including PLSR, SVR and RFR. The model performance (R^2 and *RRMSE*) of three modelling approaches is ranked by critical difference diagrams, in which the lower the rank (closer to the left) the better the modelling approach performs. Groups of R^2 or *RRMSE* that are not significantly different (Nemenyi pos-hoc test, p > 0.05) are connected by horizontal lines.

4. Results

4.1. Comparison of model performance across nutrients

Model performance (i.e., validation R^2 and RRMSE) was significantly different among 12 foliar nutrients (Welch ANOVA, p < 0.001; Fig. 2A). Specifically, the performance difference among foliar nutrients was consistent between Planet-4 and Sentinel-2, as well as between Planet-8 and PRISMA. In the Planet-4 and Sentinel-2 derived models, N was best predicted (average R^2 and RRMSE: 0.77, 15 % for Planet-4 and Sentinel-2), followed by macronutrients S (0.63, 11 % for Planet-4; 0.60, 11 % for Sentinel-2), Mg (0.58, 11 % for Planet-4; 0.65, 10 % for Sentinel-2), Ca (0.51, 9 % for Planet-4; 0.49, 9 % for Sentinel-2), Na (0.69, 22 % for Planet-4 and Sentinel-2), P (0.49, 9 % for Planet-4 and Sentinel-2) and K (0.20, 8 % for Planet-4 and Sentinel-2), and then by all micronutrients $R^2 = 0.04 \sim 0.61$; $RRMSE = 16 \% \sim 28 \%$). In the Planet-8 and PRISMA

derived models, macronutrients (i.e., N, P, K, Mg, Ca, S and Na) had lower R^2 and RRMSE ($R^2=0.06\sim0.59$; $RRMSE=7\%\sim57$ %) than micronutrients (i.e., Fe, Mn, B, Cu and Zn: $R^2=0.18\sim0.60$; $RRMSE=19\%\sim66\%$).

Macronutrients were generally more predictable compared to micronutrients (Fig. 2B). In the PlanetScope-4 and Sentinel-2 derived models, macronutrients had a significantly higher R^2 (Mann-Whitney U test: p < 0.05 for PlanetScope-4; p < 0.001 for Sentinel-2) and a significantly lower RRMSE (p < 0.001 for both satellites) than micronutrients. In the PlanetScope-8 and PRISMA derived models, both the R^2 and RRMSE for macronutrients were significantly lower than that for micronutrients (p < 0.001).

4.2. Comparison of model performance among modelling approaches

Fig. 3 presents the ranks of the overall performance of three

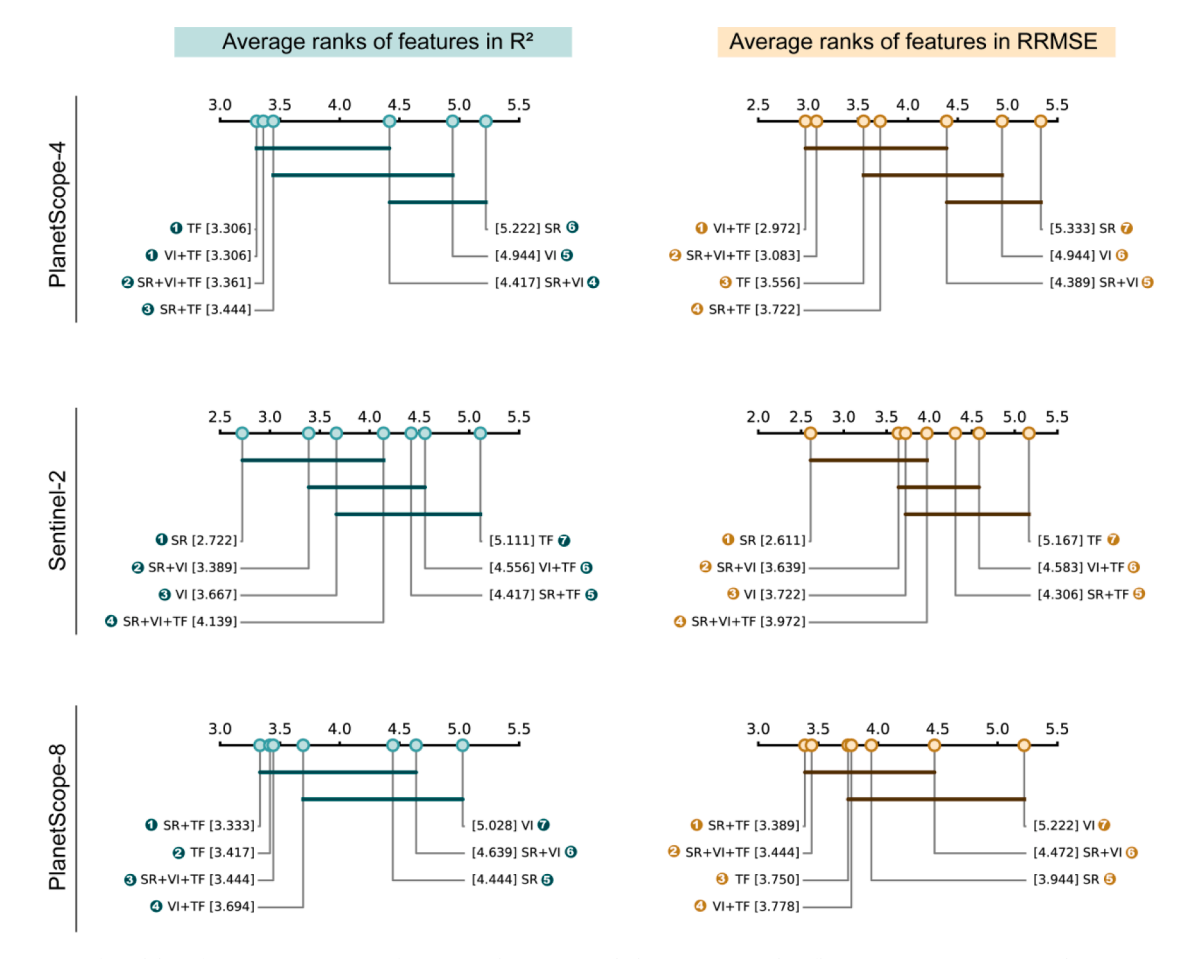


Fig. 4. Comparison of model performance using seven feature combinations, including SR (Spectral Reflectance), VI (Vegetation Index), TF (Texture Feature), SR+VI, VI+TF, SR+TF and SR+VI+TF. The model performance (R^2 and RRMSE) of using seven feature combinations is ranked by critical difference diagrams, in which the lower the rank (closer to the left) the better a model performs. Values within the round brackets are R^2 or RRMSE, while values within the square brackets are the average ranking. Groups of R^2 or RRMSE that are not significantly different (Nemenyi pos-hoc test, p=0.05) are connected by horizontal lines.

modelling approaches (i.e., PLSR, SVR and RFR) using critical difference diagrams, in which the lower the rank the better the modelling approach performs. In general, no modelling approach consistently outperformed others when using different types of satellite data as inputs. However, the ranks of three approaches were consistent between Planet-4 and Sentinel-2, as well as between Planet-8 and PRISMA. For Planet-4 and Sentinel-2, RFR significantly outperformed PLSR and SVR (Nemenyi post-hoc test: p < 0.05); PLSR and SVR did not show significant difference in model performance. For Planet-8, the R^2 of RFR and SVR were significantly better than PLSR, whereas the *RRMSE* of PLSR and SVR were significantly better than RFR. For PRISMA, no modelling approach outperformed others.

4.3. Comparison of model performance using different feature combinations

Fig. 4 ranks the performance of the PlanetScope-4, Sentinel-2 and PlanetScope-8 derived feature combinations in modelling nutrients. These feature combinations included SR (spectral reflectance), VI (vegetation indices), TF (texture features), SR+VI, VI+TF, SR+TF and

SR+VI+TF. For PlanetScope-4 and PlanetScope-8, models using texture features (i.e., TF, VI+TF, SR+TF and SR+VI+TF) consistently outperformed those models not using texture features (i.e., SR, VI and SR+VI) ("PlanetScope-4" and "PlanetScope-8" in Fig. 4). For Sentinel-2, for feature combinations ranks seven SR>SR+VI>VI>SR+VI+TF>SR+TF>VI+TF>TF("Sentinel-2" Fig. 4). In other words, models not using texture features (i.e., SR, VI and SR+VI) outperformed those models using texture features (i.e., TF, VI+TF, SR+TF and SR+VI+TF). In terms of the ranks for models using only one type of features as inputs (i.e., SR, TF or VI), it was TF>VI>SR for PlanetScope-4, TF>SR>VI for PlanetScope-8, and SR>VI>TF for Sentinel-2. The optimal feature combination was SR for PRIMSA and Sentinel-2, and TF for PlanetScope-4 and -8.

4.4. Selection of important input features

Fig. 5 and Fig. 6 present the feature importance scores for the optimal PRIMSA and Sentinel-2 derived models, and the optimal PlanetScope-4 and 8 derived models, respectively. The three modelling approaches (i. e., PLSR, SVR and RFR) tended to have different patterns of selecting

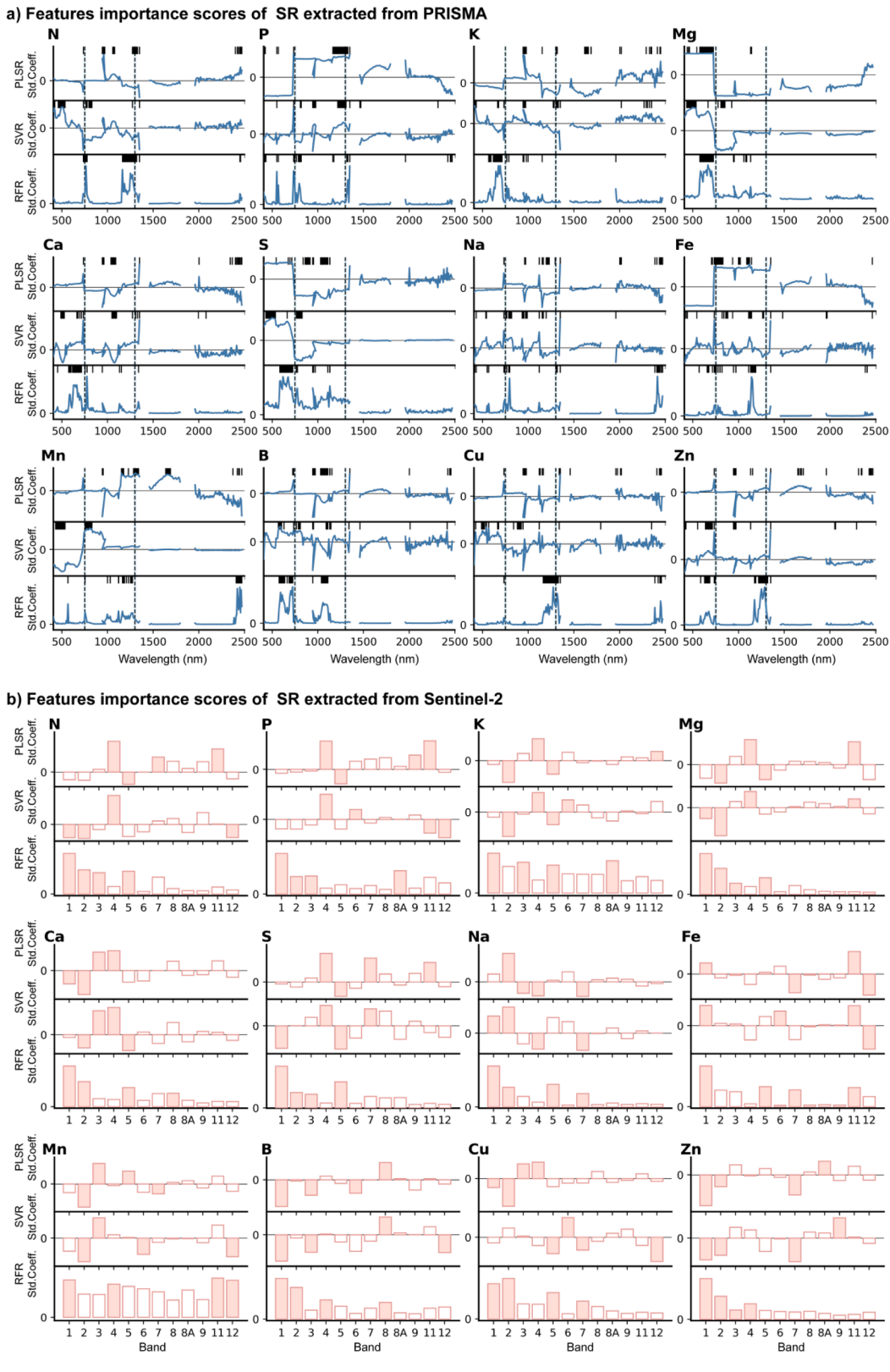


Fig. 5. Feature importance scores for the optimal PRISMA and Sentinel-2 derived models. Spectral reflectance (SR) is used as model inputs. In panel A, the absolute feature importance scores at PRISMA bands are sorted in descending order, and then the top 10 % ranked bands are chosen as important bands (represented by the solid and short vertical lines). The long and dashed vertical lines indicate the separation of visible (i.e., 400–750 nm), near infrared (i.e., 750–1300 nm) and shortwave infrared (i.e., 1300–2500 nm) wavelength regions. In panel B, the absolute feature importance scores at Sentinel-2 bands are sorted in descending order, and then the top four ranked bands are chosen as important bands (represented by the color filled bars).

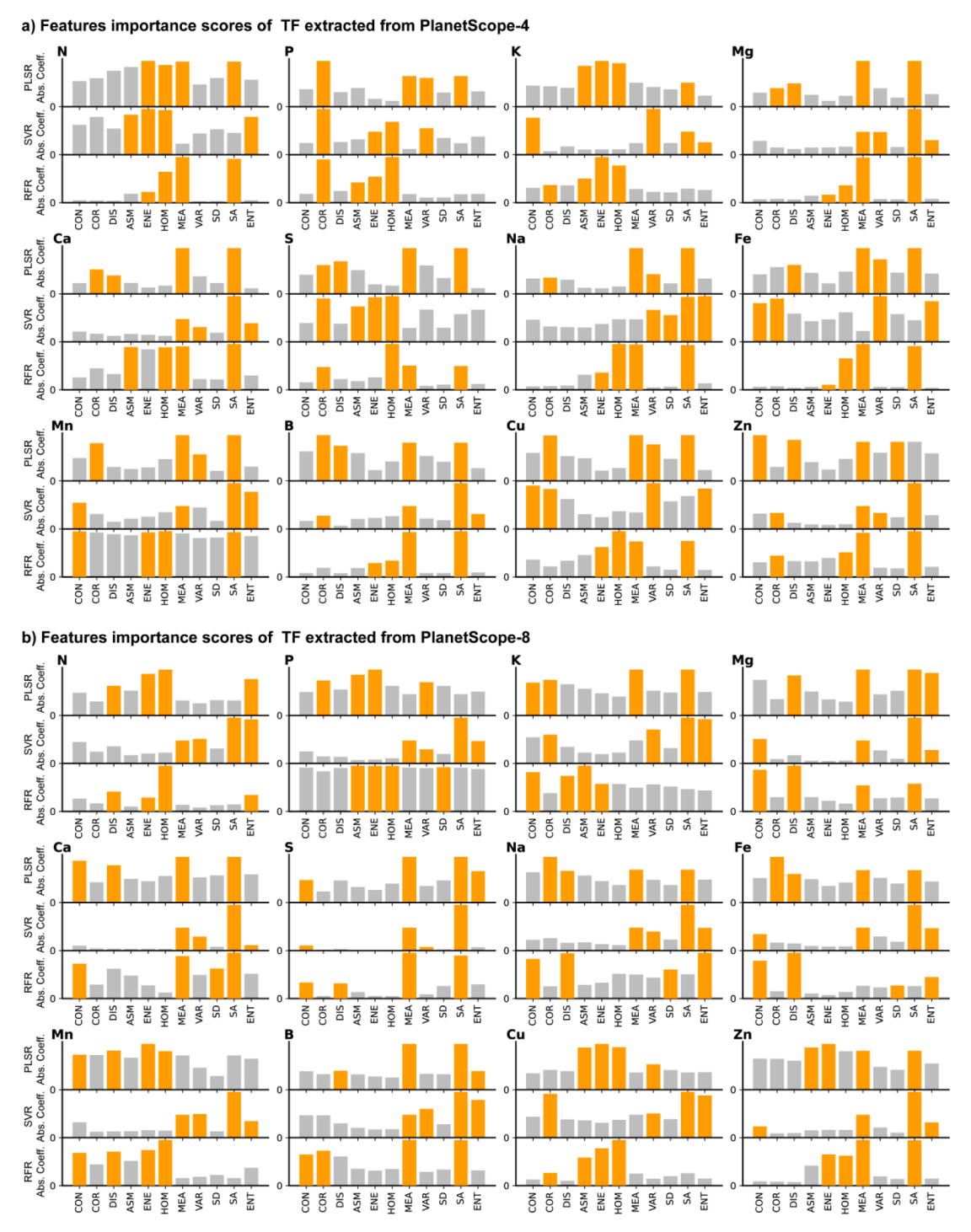


Fig. 6. Feature importance scores for the optimal PlanetScope-4 and -8 derived models. Texture features (TF) are used as model inputs. The absolute feature importance scores at PlanetScope-4/8 derived TFs are ranked in descending order, and the top four ranked features are selected as important features (represented by the color filled bars).

important features. For example, the important bands identified by the PRIMSA derived PLSR models for foliar N were clustered around 950, 1050 and 1300 nm in the NIR region, 2450 nm in the SWIR region; the important bands selected by SVR were clustered around 450 and 530 nm in the VIS region, 750 and 820 nm in the near infrared wavelength region; the important bands selected by RFR were clustered around 750, 1200–1300 nm in the near infrared wavelength region (Fig. 5A). Similarly, in the optimal Sentinel-2 derived models for foliar N, PLSR

identified bands 4 (central wavelength: 664 nm), 5 (703 nm), 7 (780 nm) and 11 (1612 nm) as important bands; SVR identified bands at 442 nm, 492 nm, 664 nm and 2201 nm as important bands; RFR identified bands at 442 nm, 492 nm, 559 nm and 704 nm as important bands (Fig. 5B).

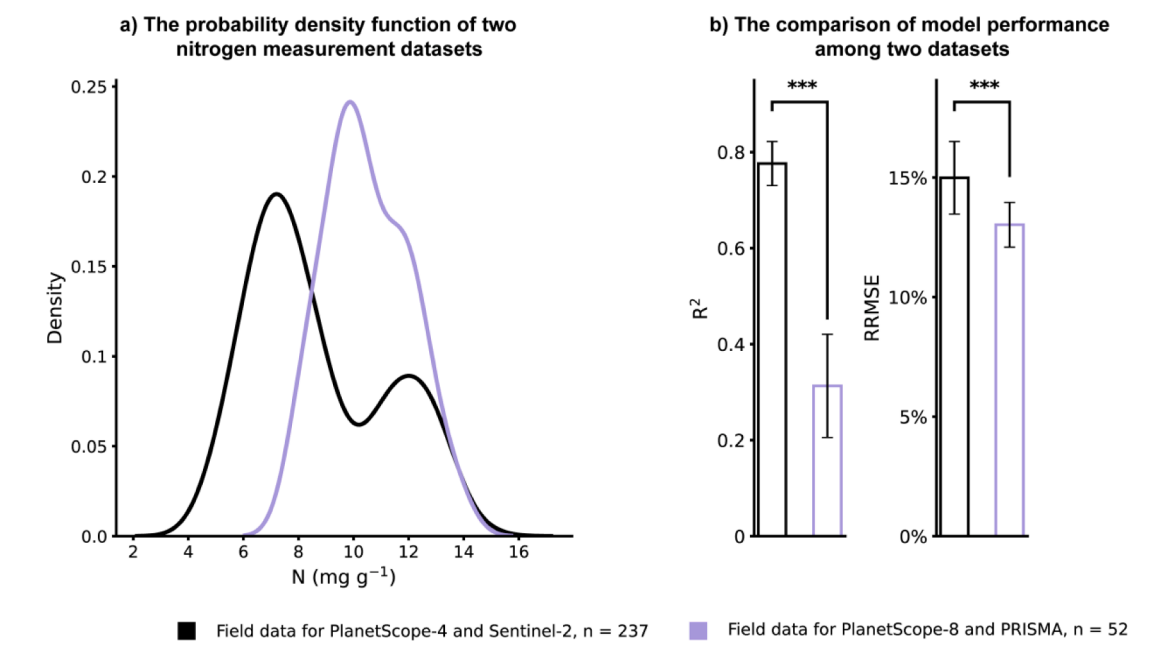


Fig. 7. The influence of data availability on the predictability of foliar nitrogen. Panel A shows the data distribution of field nitrogen measurements used to calibrate nutrient models from PlanetScope-4 and Sentinel-2 images, as well as PlanetScope-8 and PRISMA images, respectively. Panel B shows the comparison of average model accuracy (R^2 and RRMSE) between two datasets. Student's t-test indicates that the model accuracy derived from PlanetScope-4 and Sentinel-2 images was significantly higher than that from PlanetScope-8 and PRISMA images (p < 0.001).

5. Discussion

5.1. The physical mechanism of remote sensing of foliar nutrients

The predictability of nutrients in cranberry foliage was mainly affected by the correlations between nutrients and the input features of prediction models. As indicated by Appendix, those foliar nutrients (e.g., N, Mg, Ca and S in "PlanetScope-4" in Appendix) having a stronger correlation with model inputs generally had a higher validation model R^2 and a lower RRMSE (e.g., N, Mg, Ca and S in "PlanetScope-4" in Fig. 2). It should be noted that the strong correlation observed between foliar nutrients and model input features does not necessarily imply a direct causal relationship between them.

Except for nitrogen, most foliar nutrients do not exhibit distinct absorptions associated with C, H, N or O molecular bonds in 400–2500 nm (Liu et al., 2023; Pandey et al., 2017; Singh et al., 2022). Even for foliar nitrogen, its absorption features within the shortwave infrared range (i. e., N–H, stretch at 1510 nm, C–H stretch at 1690 nm, O–H stretch and deformation at 1940 nm, N=H bend and N–H stretch at 2060 nm, C-N stretch at 2180 nm, N–H stretch at 2300 nm and C–H deformation at 2350 nm) can be masked by the absorptions of other leaf biochemicals such as leaf water and dry matters (e.g., cellulose, starch, sugar and lignin) (Bhattarai et al., 2023; Curran, 1989). Consequently, variations in most foliar nutrients within leaves are unlikely to directly impact leaf or canopy reflectance.

The correlation between nutrients and leaf/canopy spectra is mainly attributed to the correlation between nutrients and those leaf components (e.g., pigments, water and dry matter) that do have spectral features within 400–2500 nm (Bhattarai et al., 2023; Chlus and Townsend, 2022; Liu et al., 2023; Mutanga et al., 2005; Pandey et al., 2017;

Pullanagari et al., 2016; Singh et al., 2022). One example could be found from the prediction of foliar magnesium: Mg is an crucial element within the chlorophyll molecule, and correlates well with leaf chlorophyll (Liu et al., 2023). Therefore, the successful retrieval of foliar Mg from PlanetScope-4 and Sentinel-2 imagery (average $R^2=0.58\sim65$, RRMSE=11 %; Fig. 2) was mainly attributed to the correlation between Mg and the chlorophyll absorption features within 400–800 nm. Similarly, in a recent study by Bhattarai et al. (2023) on spruce forests, foliar equivalent water thickness (EWT) was found to be significantly correlated with several foliar nutrients, including N (Pearson's correlation r=0.82), P (0.82), K (0.55), Cu (0.51) and Fe (0.47). It should also be noted that the correlation between nutrients and the above-mentioned leaf components may vary with plant species, study sites and phenological stages (Berger et al., 2020; Chlus and Townsend, 2022; Liu et al., 2023; Pullanagari et al., 2016).

5.2. The influence of data availability on model performance

As opposed to our expectation, the models derived from PlanetScope-8 and PRISMA did not outperform those from PlanetScope-4 and Sentinel-2, despite having more spectral bands. Data availability may be the main reason for this.

In this study, foliar nutrients were collected for both the early (dates from late June to early July, including 2018–07-03, 2019–06-26 and 2021–06-22) and late (dates from middle August to early September, including 2019–09-04, 2020–08-15 and 2021–08-15) crop growth stages. Since PlanetScope-8 and PRISMA (2021–06-22 and 2021–08-15) had less clear-sky images than PlanetScope-4 and Sentinel-2 (2018–07-03, 2019–06-26, 2021–06-22, 2019–09-04 and 2020–08-15) (Fig. 1), the dataset size used for building nutrient models from PlanetScope-8

and PRISMA (n=52) data was much less than that from PlanetScope-4 and Sentinel-2 data (n=237). This difference in data availability yielded a narrower nutrient range (nitrogen range: $6-16~{\rm mg\cdot g}^{-1}$; Fig. 7A) and a lower prediction accuracy (R^2 and RRMSE: 0.31 and 11 %; Fig. 7B) for PlanetScope-4 and Sentinel-2. Considering that PlanetScope-8 and PRISMA provide more spectral bands than PlanetScope-4 and Sentinel-2, the model accuracy derived from them would be better than that derived from PlanetScope-4 and Sentinel-2 when the same field dataset is used for building models.

It needs to be noted that the effect of data availability on the predictability of foliar nutrients can be complicated by crop growth stages. In other words, the prediction accuracy of foliar nutrients can be greatly reduced if data cannot be collected at critical growth stages. For example, many studies have found that the correlation between crop nitrogen and canopy spectra at early growth stages was much stronger than that at reproductive stages when nitrogen was reallocated from leaves to other plant organs (Berger et al., 2020; Masclaux-Daubresse et al., 2010; Milla et al., 2005). Therefore, a decrease in model prediction was observed when data were less available from early growth stages (Fig. 2).

5.3. The effect of imagery characteristics on the predictability of foliar nutrients

The advantages of leveraging multi-source satellite remote sensing to map foliar nutrients depend on imagery characteristics, more specifically, on the spectral and spatial resolutions of satellite images. In this study, the fine resolution (~3 m) of PlanetScope-4 and PlanetScope-8 images was able to characterize the foliar nutrient variation within each cranberry bed (\sim 50 \times 300 m). Therefore, feature combinations using texture features (i.e., TF, SR+TF, VI+TF and SR+VI+TF; TF: texture features; SR: surface reflectance; VI: vegetation indices) generally had a better prediction accuracy than those combinations not using texture features ("PlanetScope-4" and "PlanetScope-8" in Fig. 4). In contrast, texture features did not output other features (SR and VI) for Sentinel-2 and PRISMA images since their spatial resolutions (Sentinel-2: 10, 20 and 60 m; PRISMA 30 m) exhibited limited capability in capturing spatial variations within cranberry beds. Sentinel-2 and PRISMA demonstrated that the full-spectral surface reflectance within the 400-2500 nm range was adequate for modeling foliar nutrients. The incorporation of vegetation indices and texture features into the model inputs did not result in a discernible improvement in prediction accuracy ("Sentinle-2" in Fig. 4).

In this study, the capability of PlanetScope, Sentinel-2, and PRISMA images to quantify foliar nutrients was evaluated separately. Each satellite sensor offers distinct advantages in terms of spatial and spectral resolution. However, future efforts could focus on fusing these multisource images to achieve higher spatial and spectral resolutions, as suggested by Yokoya et al. (2017). By combining the high spatial resolution of PlanetScope, the moderate spatial and spectral resolution of Sentinel-2, and the superior spectral resolution of PRISMA, we can create a comprehensive dataset that leverages the strengths of each sensor. This fusion approach is believed to enable detailed and accurate mapping of foliar nutrients in heterogeneous landscapes or small-scale agricultural fields. It will enhance our understanding and management of foliar nutrients in diverse environments.

6. Conclusion

We investigated the capability of multi-source satellite images (PlanetScope, Sentinel-2 and PRISMA) to map 12 foliar nutrients in cranberries. Different groups of input features (i.e., spectral reflectance (SR), vegetation indices (VI) and texture features (TF)) and their combinations were tested by three data-driven models (PLSR, SVR and RFR) for their capability of predicting foliar nutrients. Our results indicated that the prediction accuracy was significantly different among foliar nutrients. The optimal features for predicting nutrients depended on the characteristics of satellite images. For PlanetScope images, features containing with TF demonstrated a better performance. As for the images with more spectral information (i.e., Sentinel-2 and PRISMA), spectra related features (i.e., SR and VI) exhibited a better performance. In terms of the comparison across different modelling approaches, no modelling approach consistently outperformed others. The successful retrieval of foliar nutrients from satellite imagery was influenced by many factors, including the correlation between nutrients and model inputs, the data availability at critical growth stages, and satellite image characteristics.

CRediT authorship contribution statement

Yurong Huang: Writing – review & editing, Writing – original draft, Methodology, Investigation, Formal analysis, Data curation, Conceptualization. Nanfeng Liu: Writing – review & editing, Writing – original draft, Visualization, Validation, Methodology, Investigation, Funding acquisition, Formal analysis, Data curation, Conceptualization. Erin Wagner Hokanson: Writing – review & editing, Project administration, Data curation. Nicole Hansen: Writing – review & editing, Data curation. Philip A. Townsend: Writing – review & editing, Funding acquisition, Conceptualization.

Declaration of competing interest

The authors declare that they have no known competing financial interests or personal relationships that could have appeared to influence the work reported in this paper.

Data availability

The authors do not have permission to share data.

Acknowledgement

PAT received research funding from the Wisconsin State Cranberry Growers Association, the Cranberry Institute and Ocean Spray. NL received research funding from GuangDong Basic and Applied Basic Research Foundation (2022A1515110575, 2023A1515011406), Guangzhou Key Research and Development Program (2024B03J1266), Fundamental Research Funds for the Central Universities, Sun Yat-sen University (24qnpy016) and funding from NSF ASCEND Biology Integration Institute grant (DBI-2021898) and NSF Early NEON science grant (1638720). Additional support to the project was provided by USDA Hatch and McIntire-Stennis WIS03079 and WIS03008. Thank you to Joel Cryer, Benjamin Spaier and Cecilia Vanden Heuvel for assistance with field data collection and processing.

Appendix

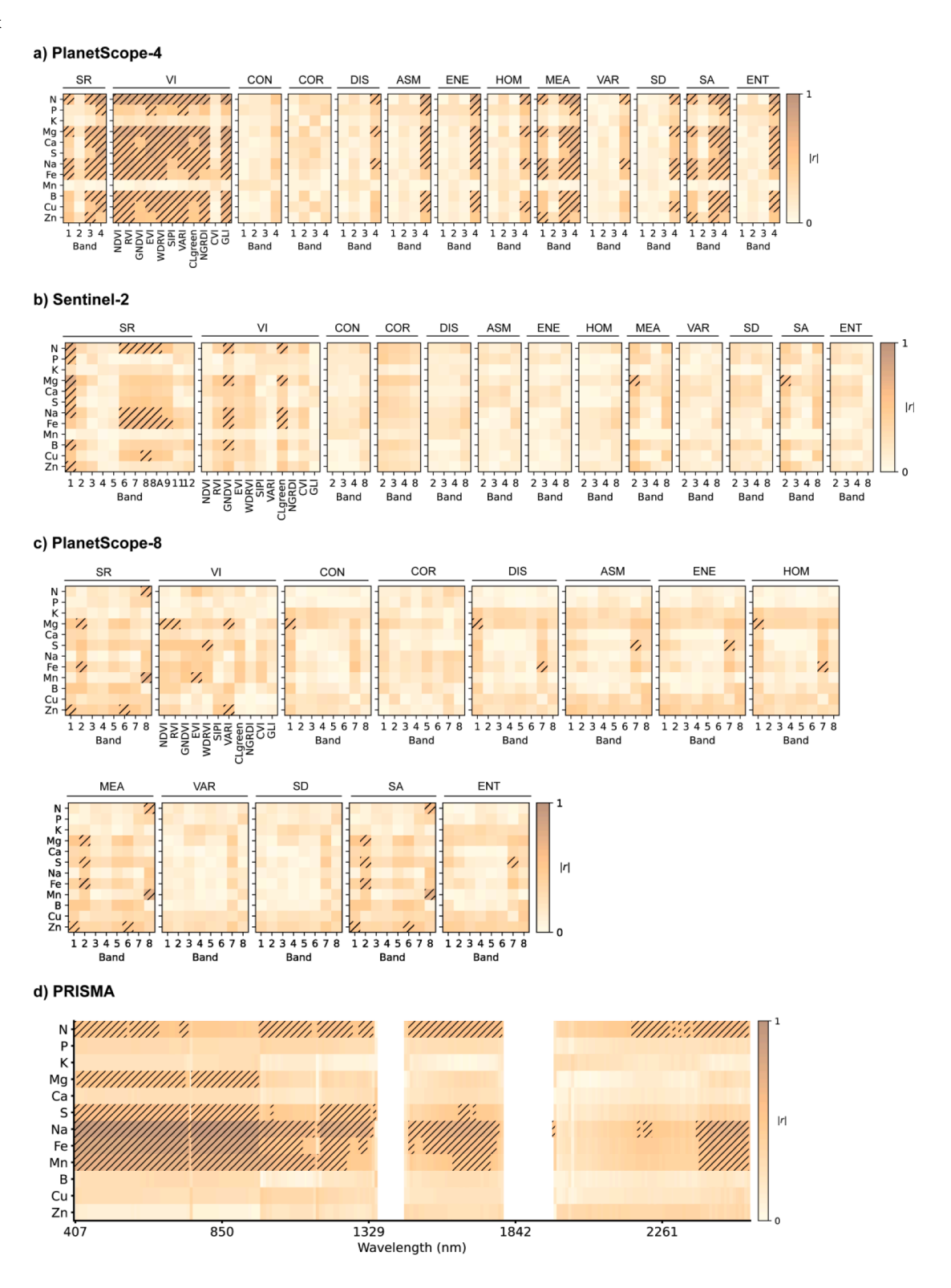


Fig. A1. The absolute Pearson's correlations (|r|) between nutrients and input features of prediction models. SR: spectral reflectance; VI: vegetation indices. Explanations of texture features CON, COR, DIS, ASM, ENE, HOM, MEA, VAR, SD, SA and ENT can be found from . Strong correlations (|r|>0.5) are highlighted by forward slashes.

References

- Adhikari, R., Li, C., Kalbaugh, K., Nemali, K., 2020. A low-cost smartphone controlled sensor based on image analysis for estimating whole-plant tissue nitrogen (N) content in floriculture crops. Comput. Electron. Agric. 169, 105173 https://doi.org/ 10.1016/j.compag.2019.105173.
- Amanullah (Ed.), 2020. Agronomy: climate change & food security. IntechOpen, London, United Kingdom.
- Barker, A.V., Pilbeam, D.J. (Eds.), 2015. Handbook of Plant Nutrition, Second, edition. ed. CRC Press/Taylor & Francis Group, Boca Raton, FL.
- Belgiu, M., Drăgut, L., 2016. Random forest in remote sensing: a review of applications and future directions. ISPRS J. Photogramm. Remote Sens. 114, 24–31. https://doi. org/10.1016/j.isprsiprs.2016.01.011.
- Belgiu, M., Marshall, M., Boschetti, M., Pepe, M., Stein, A., Nelson, A., 2023. PRISMA and Sentinel-2 spectral response to the nutrient composition of grains. Remote Sens. Environ. 292, 113567 https://doi.org/10.1016/j.rse.2023.113567.
- Berger, K., Verrelst, J., Féret, J.-B., Wang, Z., Wocher, M., Strathmann, M., Danner, M., Mauser, W., Hank, T., 2020. Crop nitrogen monitoring: recent progress and principal developments in the context of imaging spectroscopy missions. Remote Sens. Environ. 242, 111758 https://doi.org/10.1016/j.rse.2020.111758.
- Bhattarai, R., Rahimzadeh-Bajgiran, P., Mech, A., 2023. Estimating nutritive, non-nutritive and defense foliar traits in spruce-fir stands using remote sensing and site data. For. Ecol. Manag. 549, 121461 https://doi.org/10.1016/j. foreco.2023.121461.
- Brown, P.H., Zhao, F.-J., Dobermann, A., 2022. What is a plant nutrient? Changing definitions to advance science and innovation in plant nutrition. Plant Soil 476, 11–23. https://doi.org/10.1007/s11104-021-05171-w
- Campos-Soriano, L., Bundó, M., Bach-Pages, M., Chiang, S., Chiou, T., San Segundo, B.,
 2020. Phosphate excess increases susceptibility to pathogen infection in rice. Mol.
 Plant Pathol. 21, 555–570. https://doi.org/10.1111/mpp.12916.
 Cao, Q., Yang, G., Duan, D., Chen, L., Wang, F., Xu, B., Zhao, C., Niu, F., 2022. Combining
- Cao, Q., Yang, G., Duan, D., Chen, L., Wang, F., Xu, B., Zhao, C., Niu, F., 2022. Combining multispectral and hyperspectral data to estimate nitrogen status of tea plants (Camellia sinensis (L.) O. Kuntze) under field conditions. Comput. Electron. Agric. 198, 107084 https://doi.org/10.1016/j.compag.2022.107084.
- Chlus, A., Townsend, P.A., 2022. Characterizing seasonal variation in foliar biochemistry with airborne imaging spectroscopy. Remote Sens. Environ. 275, 113023 https:// doi.org/10.1016/j.rse.2022.113023.
- Cogliati, S., Sarti, F., Chiarantini, L., Cosi, M., Lorusso, R., Lopinto, E., Miglietta, F., Genesio, L., Guanter, L., Damm, A., Pérez-López, S., Scheffler, D., Tagliabue, G., Panigada, C., Rascher, U., Dowling, T.P.F., Giardino, C., Colombo, R., 2021. The PRISMA imaging spectroscopy mission: overview and first performance analysis. Remote Sens. Environ. 262, 112499 https://doi.org/10.1016/j.rse.2021.112499.
- Connor, D.J., Loomis, R.S., Cassman, K.G., Loomis, R.S., 2011. Crop ecology: Productivity and management in agricultural systems, 2nd ed. Cambridge University Press, Cambridge, New York.
- Curran, P.J., 1989. Remote sensing of foliar chemistry. Remote Sens. Environ. 30, 271–278. https://doi.org/10.1016/0034-4257(89)90069-2.
- Pereira, F.R. da S., de Lima, J.P., Freitas, R.G., Dos Reis, A.A., Amaral, L.R. do, Figueiredo, G.K.D.A., Lamparelli, R.A.C., Magalhães, P.S.G., 2022. Nitrogen variability assessment of pasture fields under an integrated crop-livestock system using UAV, PlanetScope, and Sentinel-2 data. Comput. Electron. Agric. 193, 106645. doi: 10.1016/j.compag.2021.106645.
- Darvishzadeh, R., Skidmore, A., Abdullah, H., Cherenet, E., Ali, A., Wang, T., Nieuwenhuis, W., Heurich, M., Vrieling, A., O'Connor, B., Paganini, M., 2019. Mapping leaf chlorophyll content from Sentinel-2 and RapidEye data in spruce stands using the invertible forest reflectance model. Int. J. Appl. Earth Obs. Geoinformation 79, 58–70. https://doi.org/10.1016/j.jag.2019.03.003.
- de Bang, T.C., Husted, S., Laursen, K.H., Persson, D.P., Schjoerring, J.K., 2021. The molecular-physiological functions of mineral macronutrients and their consequences for deficiency symptoms in plants. New Phytol. 229, 2446–2469. https://doi.org/10.1111/nph.17074.
- Delloye, C., Weiss, M., Defourny, P., 2018. Retrieval of the canopy chlorophyll content from Sentinel-2 spectral bands to estimate nitrogen uptake in intensive winter wheat cropping systems. Remote Sens. Environ. 216, 245–261. https://doi.org/10.1016/j. rss. 2018.06.037
- Fan, Y., Feng, H., Yue, J., Jin, X., Liu, Y., Chen, R., Bian, M., Ma, Y., Song, X., Yang, G., 2023. Using an optimized texture index to monitor the nitrogen content of potato plants over multiple growth stages. Comput. Electron. Agric. 212, 108147 https:// doi.org/10.1016/j.compag.2023.108147.
- Fan, K., Li, F., Chen, X., Li, Z., Mulla, D., 2022. Nitrogen balance index prediction of winter wheat by canopy hyperspectral transformation and machine learning. Remote Sens. 14, 3504. https://doi.org/10.3390/rs14143504.
- Francis, B., Aravindakumar, C.T., Brewer, P.B., Simon, S., 2023. Plant nutrient stress adaptation: a prospect for fertilizer limited agriculture. Environ. Exp. Bot. 213, 105431 https://doi.org/10.1016/j.envexpbot.2023.105431.
- Fu, Y., Yang, G., Li, Z., Song, X., Li, Z., Xu, X., Wang, P., Zhao, C., 2020. Winter wheat nitrogen status estimation using UAV-based RGB imagery and gaussian processes regression. Remote Sens. 12, 3778. https://doi.org/10.3390/rs12223778.
- Gitelson, A.A., 2004. Wide dynamic range vegetation index for remote quantification of biophysical characteristics of vegetation. J. Plant Physiol. 161, 165–173. https://doi. org/10.1078/0176-1617-01176.
- Gitelson, A.A., Kaufman, Y.J., Stark, R., Rundquist, D., 2002. Novel algorithms for remote estimation of vegetation fraction. Remote Sens. Environ. 80, 76–87. https:// doi.org/10.1016/S0034-4257(01)00289-9.
- Gitelson, A.A., Gritz, Y., Merzlyak, M.N., 2003. Relationships between leaf chlorophyll content and spectral reflectance and algorithms for non-destructive chlorophyll

- assessment in higher plant leaves. J. Plant Physiol. 160, 271–282. https://doi.org/
- Huete, A., 1997. A comparison of vegetation indices over a global set of TM images for EOS-MODIS. Remote Sens. Environ. 59, 440–451. https://doi.org/10.1016/S0034-4257(06)00112-5
- Huete, A., Didan, K., Miura, T., Rodriguez, E.P., Gao, X., Ferreira, L.G., 2002. Overview of the radiometric and biophysical performance of the MODIS vegetation indices. Remote Sens. Environ. 83, 195–213. https://doi.org/10.1016/S0034-4257(02) 00096-2
- Inoue, Y., Sakaiya, E., Zhu, Y., Takahashi, W., 2012. Diagnostic mapping of canopy nitrogen content in rice based on hyperspectral measurements. Remote Sens. Environ. 126, 210–221. https://doi.org/10.1016/j.rse.2012.08.026.
- Jones, J.B., Case, V.W., 1990. In: Sampling, Handling, and Analyzing Plant Tissue Samples. SSSA Book Series. Soil Science Society of America, Madison, WI, USA, pp. 389–427. https://doi.org/10.2136/sssabookser3.3ed.c15.
- Kirkby, E.A., 2023. Introduction, definition, and classification of nutrients, in: Marschner's Mineral Nutrition of Plants. Elsevier, pp. 3–9. doi: 10.1016/B978-0-12-819773-8.00016-2.
- Planet Labs, 2022. Planet imagery product specifications.
- Li, Z., Zhang, R., Xia, S., Wang, L., Liu, C., Zhang, R., Fan, Z., Chen, F., Liu, Y., 2019. Interactions between N, P and K fertilizers affect the environment and the yield and quality of satsumas. Glob. Ecol. Conserv. 19, e00663.
- Liu, S., Li, L., Gao, W., Zhang, Y., Liu, Y., Wang, S., Lu, J., 2018. Diagnosis of nitrogen status in winter oilseed rape (Brassica napus L.) using in-situ hyperspectral data and unmanned aerial vehicle (UAV) multispectral images. Comput. Electron. Agric. 151, 185–195. https://doi.org/10.1016/j.compag.2018.05.026.
- Liu, N., Townsend, P.A., Naber, M.R., Bethke, P.C., Hills, W.B., Wang, Y., 2021. Hyperspectral imagery to monitor crop nutrient status within and across growing seasons. Remote Sens. Environ. 255, 112303 https://doi.org/10.1016/j. rse.2021.112303.
- Liu, N., Wagner Hokanson, E., Hansen, N., Townsend, P.A., 2023. Multi-year hyperspectral remote sensing of a comprehensive set of crop foliar nutrients in cranberries. ISPRS J. Photogramm. Remote Sens. 205, 135–146. https://doi.org/ 10.1016/j.isprsjprs.2023.10.003.
- Louhaichi, M., Borman, M.M., Johnson, D.E., 2001. Spatially located platform and aerial photography for documentation of grazing impacts on wheat. Geocarto Int. 16, 65–70. https://doi.org/10.1080/10106040108542184.
- Marschner, H., 1995. Mineral nutrition of higher plants, 2nd, edition. ed. Academic Press. London San Diego.
- Masclaux-Daubresse, C., Daniel-Vedele, F., Dechorgnat, J., Chardon, F., Gaufichon, L., Suzuki, A., 2010. Nitrogen uptake, assimilation and remobilization in plants: challenges for sustainable and productive agriculture. Ann. Bot. 105, 1141–1157. https://doi.org/10.1093/aob/mcq028.
- Milla, R., Castro-Díez, P., Maestro-Martínez, M., Montserrat-Martí, G., 2005.
 Relationships between phenology and the remobilization of nitrogen, phosphorus and potassium in branches of eight Mediterranean evergreens. New Phytol. 168, 167–178. https://doi.org/10.1111/j.1469-8137.2005.01477.x.
- Mortvedt, J.J. (Ed.), 1991. Micronutrients in agriculture, 2nd ed. ed, The Soil Science Society of America book series. Soil Science Society of America, Madison, Wis., USA.
- Muñoz-Huerta, R., Guevara-Gonzalez, R., Contreras-Medina, L., Torres-Pacheco, I., Prado-Olivarez, J., Ocampo-Velazquez, R., 2013. A review of methods for sensing the nitrogen status in plants: advantages, disadvantages and recent advances. Sensors 13, 10823–10843. https://doi.org/10.3390/s130810823.
- Mutanga, O., Skidmore, A.K., Kumar, L., Ferwerda, J., 2005. Estimating tropical pasture quality at canopy level using band depth analysis with continuum removal in the visible domain. Int. J. Remote Sens. 26, 1093–1108. https://doi.org/10.1080/ 01431160512331326738.
- Osco, L.P., Junior, J.M., Ramos, A.P.M., Furuya, D.E.G., Santana, D.C., Teodoro, L.P.R., Gonçalves, W.N., Baio, F.H.R., Pistori, H., Junior, C.A. da S., Teodoro, P.E., 2020. Leaf nitrogen concentration and plant height prediction for maize using UAV-based multispectral imagery and machine learning techniques. Remote Sens. 12, 3237. doi: 10.3390/rs12193237.
- Pandey, P., Ge, Y., Stoerger, V., Schnable, J.C., 2017. High throughput in vivo analysis of plant leaf chemical properties using hyperspectral imaging. Front. Plant Sci. 8, 1348. https://doi.org/10.3389/fpls.2017.01348.
- Pen Uelas, J., Filella, I., Lloret, P., Mun Oz, F., Vilajeliu, M., 1995. Reflectance assessment of mite effects on apple trees. Int. J. Remote Sens. 16, 2727–2733. https://doi.org/ 10.1080/01431169508954588.
- Pullanagari, R.R., Kereszturi, G., Yule, I.J., 2016. Mapping of macro and micro nutrients of mixed pastures using airborne AisaFENIX hyperspectral imagery. ISPRS J. Photogramm. Remote Sens. 117, 1–10. https://doi.org/10.1016/j. isprsiors.2016.03.010.
- Rouse, J.W., Haas, R.H., Schell, J.A., Deering, D.W., 1973. Monitoring vegetation systems in the great plains with ERTS.
- Roy, D.P., Huang, H., Houborg, R., Martins, V.S., 2021. A global analysis of the temporal availability of PlanetScope high spatial resolution multi-spectral imagery. Remote Sens. Environ. 264, 112586 https://doi.org/10.1016/j.rse.2021.112586.
- Sarkar, S., Sagan, V., Bhadra, S., Rhodes, K., Pokharel, M., Fritschi, F.B., 2023. Soybean seed composition prediction from standing crops using PlanetScope satellite imagery and machine learning. ISPRS J. Photogramm. Remote Sens. 204, 257–274. https:// doi.org/10.1016/j.isprsjprs.2023.09.010.
- Sharifi, A., 2020. Using sentinel-2 data to predict nitrogen uptake in maize crop. IEEE J. Sel. Top. Appl. Earth Obs. Remote Sens. 13, 2656–2662. https://doi.org/10.1109/ ISTARS 2020 2998638
- Singh, L., Mutanga, O., Mafongoya, P., Peerbhay, K., Crous, J., 2022. Hyperspectral remote sensing for foliar nutrient detection in forestry: a near-infrared perspective.

- Remote Sens. Appl. Soc. Environ. 25, 100676 https://doi.org/10.1016/j.rsase.2021.100676.
- Taiz, L., Zeiger, E., 2010. Plant physiology, 5th ed. Sinauer Associates, Sunderland, MA.
 Thapa, S., Bhandari, A., Ghimire, R., Xue, Q., Kidwaro, F., Ghatrehsamani, S.,
 Maharjan, B., Goodwin, M., 2021. Managing micronutrients for improving soil fertility, health, and soybean yield. Sustainability 13, 11766. https://doi.org/10.3200/srs12311766
- Tucker, C.J., 1979. Red and photographic infrared linear combinations for monitoring vegetation. Remote Sens. Environ. 8, 127–150. https://doi.org/10.1016/0034-4257 (79)90013-0.
- Van Maarschalkerweerd, M., Husted, S., 2015. Recent developments in fast spectroscopy for plant mineral analysis. Front. Plant Sci. 6 https://doi.org/10.3389/ fpls 2015.00169
- Vincini, M., Frazzi, E., D'Alessio, P., 2008. A broad-band leaf chlorophyll vegetation index at the canopy scale. Precis. Agric. 9, 303–319. https://doi.org/10.1007/ s11119-008-9075-z
- Wang, Z., Chlus, A., Geygan, R., Ye, Z., Zheng, T., Singh, A., Couture, J.J., Cavender-Bares, J., Kruger, E.L., Townsend, P.A., 2020. Foliar functional traits from imaging

- spectroscopy across biomes in eastern North America. New Phytol. 228, 494–511. $\label{eq:https:/doi.org/10.1111/nph.16711} https://doi.org/10.1111/nph.16711.$
- Weiss, M., Jacob, F., Duveiller, G., 2020. Remote sensing for agricultural applications: a meta-review. Remote Sens. Environ. 236, 111402 https://doi.org/10.1016/j. pp. 2010.111402
- Yokoya, N., Grohnfeldt, C., Chanussot, J., 2017. Hyperspectral and Multispectral Data Fusion: a comparative review of the recent literature. IEEE Geosci. Remote Sens. Mag. 5, 29–56. https://doi.org/10.1109/MGRS.2016.2637824.
- Zeng, Y., Hao, D., Huete, A., Dechant, B., Berry, J., Chen, J.M., Joiner, J., Frankenberg, C., Bond-Lamberty, B., Ryu, Y., Xiao, J., Asrar, G.R., Chen, M., 2022. Optical vegetation indices for monitoring terrestrial ecosystems globally. Nat. Rev. Earth Environ. 3, 477–493. https://doi.org/10.1038/s43017-022-00298-5.
- Zheng, H., Ma, J., Zhou, M., Li, D., Yao, X., Cao, W., Zhu, Y., Cheng, T., 2020. Enhancing the nitrogen signals of rice canopies across critical growth stages through the integration of textural and spectral information from unmanned aerial vehicle (UAV) multispectral imagery. Remote Sens. 12, 957. https://doi.org/10.3390/rs12060957.